Electronic Supplementary Material (ESI) for Materials Chemistry Frontiers.

SUPPLEMENTARY INFORMATION

Bulk $Ti_3C_2T_x$ anodes for superior sodium storage performance: The unique role of O-termination

Cong Wu[a,b], Chunfu Huang[a], Zilu Zhang[a], Yunyun Xie[a], Zhonggui Gao[b], Hai Wang[a,b*]

[a] *College of Materials Science and Engineering, Guilin University of Technology, Guilin 541004, China*

[b] *College of Physics and Technology, Guangxi Normal University, Guilin 541004, China*

[*]Corresponding author.

E-mail address: hbwanghai@gmail.com (H. Wang)

Supplementary figures

Fig. S1. (a) TEM images and (b) EDX spectra of $Ti_3C_2T_x$-VC-300 sample.

Fig. S2. TEM images of $Ti_3C_2T_x$ sample.

Fig. S3. TEM images of $Ti_3C_2T_x$-300 sample.

Fig. S4. TG-DSC measurement of $Ti_3C_2T_x$-VC-300 (a) and $Ti_3C_2T_x$-300 (b) in N_2.

Fig. S5. The adsorption-desorption isotherms of $Ti_3C_2T_x$, $Ti_3C_2T_x$-300 and $Ti_3C_2T_x$-VC-300 electrodes in N_2 (77 K) (a), and their corresponding pore size distribution (b).

Fig. S6. The cyclic voltammogram of electrodes in the first three cycles at 0.1 mV s^{-1}. (a) $Ti_3C_2T_x$ and (b) $Ti_3C_2T_x$-300.

Fig. S7. The voltage profile of $Ti_3C_2T_x$ and $Ti_3C_2T_x$-300 electrodes at different cyclic. (a) $Ti_3C_2T_x$ and (b) $Ti_3C_2T_x$-300 at 1 A g^{-1}.

Fig. S8. Cycling performance of VC-300, $Ti_3C_2T_x$, $Ti_3C_2T_x$-300 and $Ti_3C_2T_x$-VC-300 electrodes at a current density of 0.5 A g^{-1}.

Fig. S9. The long cycling performance of $Ti_3C_2T_x$, $Ti_3C_2T_x$-300 and $Ti_3C_2T_x$-VC-300 electrodes at a current density of 2 A g^{-1} after 5000 cycles.

Fig. S10. (a) GITT profiles of $Ti_3C_2T_x$, $Ti_3C_2T_x$-300 and $Ti_3C_2T_x$-VC-300 electrodes, (b) Na^+ diffusion coefficients of $Ti_3C_2T_x$, $Ti_3C_2T_x$-300, and $Ti_3C_2T_x$-VC-300 electrodes after the 3rd cycles.

Fig. S11. CV curves of the $Ti_3C_2T_x$ (a) and $Ti_3C_2T_x$-300 (b) electrode at different scan rates.

Fig. S12. The pseudocapacitive contribution (red and pink region) to the total current of $Ti_3C_2T_x$ (a) and $Ti_3C_2T_x$-300 (b) at a scan rate of 2.0 mV s^{-1}.

Fig. S13. Percentage capacitive contributions obtained at different scan rates of $Ti_3C_2T_x$ (a) and $Ti_3C_2T_x$-300 (b) at a scan rate of 0.4, 0.8, 2.0, 4.0, 8.0 and 10 mV s^{-1}.

Fig. S14. Logarithm peak current versus logarithm scan rate plots of the (a) $Ti_3C_2T_x$ and (b) $Ti_3C_2T_x$-300.

Fig. S15. XRD and corresponding SEM images of $Ti_3C_2T_x$, $Ti_3C_2T_x$-300 and $Ti_3C_2T_x$-VC-300 after 50 cycles.

Fig. S16. SEM of electrodes after 250 and 500 cycles. (a) $Ti_3C_2T_x$, (b) $Ti_3C_2T_x$-300 and (c) $Ti_3C_2T_x$-VC-300.

Fig. S17. The TEM and capacity decay mechanism of the original $Ti_3C_2T_x$ electrode after 2500 cycles at 1 A g^{-1}. (a) Low magnification TEM image, (b) Medium magnification selected area TEM image, inserting selected area polycrystalline diffraction ring, (c) Side enlarged TEM image, and (d) Schematic diagram of original $Ti_3C_2T_x$ electrode capacity attenuation mechanism.

Supplementary Notes

Note 1: Had $Ti_3C_2T_x$ been successfully obtained by the etching process?

Fig. SN1. (a) Ti_3AlC_2 precursor; (b) etched sample by HF; (c) XRD patterns of Ti_3AlC_2 and $Ti_3C_2T_x$.

Note 2. Have the VC penetrated into the interlayer of MXenes or just coated on the outside surface of the bulk MXenes during the "hot-melting decomposition process?

Fig. SN2. The FESEM images of $Ti_3C_2T_x$-VC-300 and $Ti_3C_2T_x$ under the same conditions after peeling and dispersion. (a)-(b) $Ti_3C_2T_x$-VC-300 and (c)-(d) $Ti_3C_2T_x$.

Note 3: Why the pristine $Ti_3C_2T_x$ has the highest carbon ratio?

Supplementary tables

Table S1. Changes in water contact angle of the $Ti_3C_2T_x$-VC-300 and $Ti_3C_2T_x$-300.
Table S2. Specific surface area (S_{BET}), total pore volume and average pore size of $Ti_3C_2T_x$, $Ti_3C_2T_x$-300 and $Ti_3C_2T_x$-VC-300.

Table S3. The elements percentages of $Ti_3C_2T_x$, $Ti_3C_2T_x$-300 and $Ti_3C_2T_x$-VC-300 measured with XPS.

Table S4. Summary table of electrochemical performance of $Ti_3C_2T_x$-based anodes in recent publications.

Table S5. Electrochemical data derived from EIS spectra for $Ti_3C_2T_x$, $Ti_3C_2T_x$-300 and $Ti_3C_2T_x$-VC-300.

Supplementary references

S1. Figures in supporting information

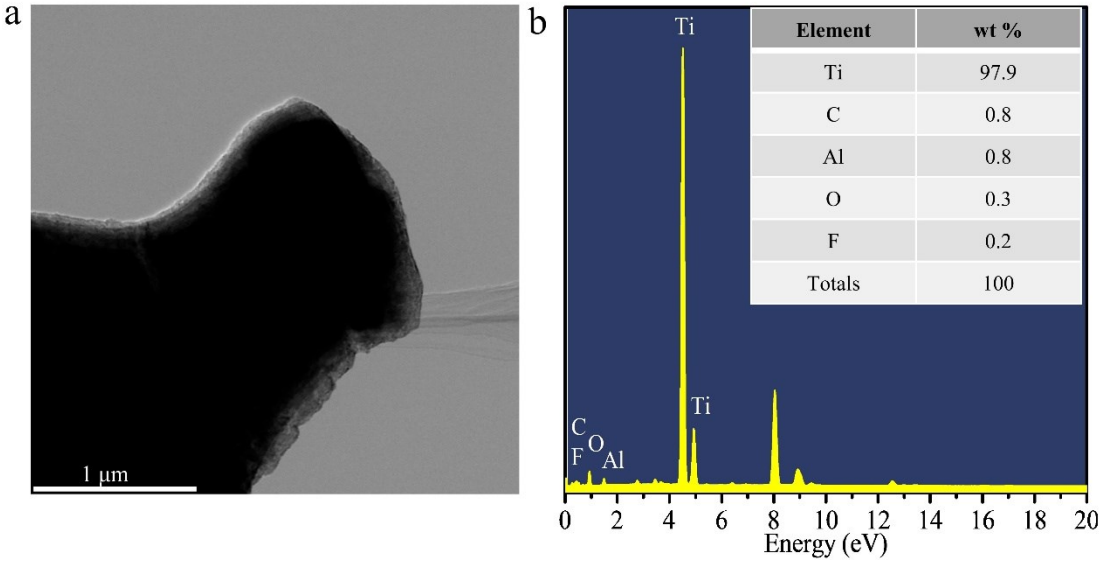

Element	wt %
Ti	97.9
C	0.8
Al	0.8
O	0.3
F	0.2
Totals	100

Figure S1 (a) TEM images and (b) EDX spectra of $Ti_3C_2T_x$-VC-300 sample.

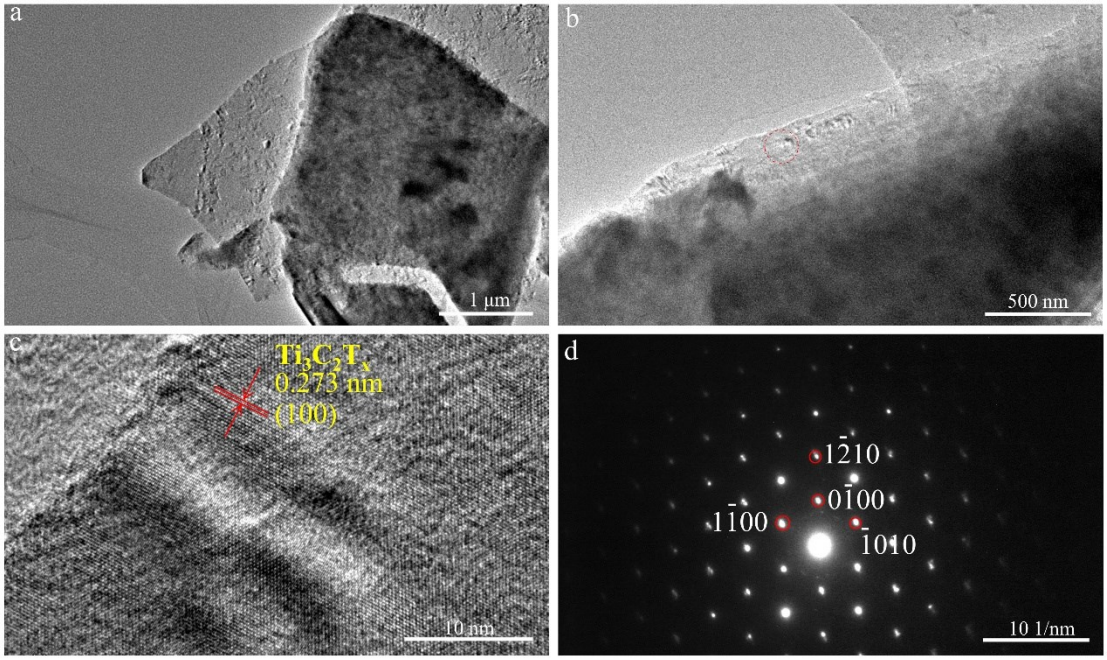

Figure S2 TEM images of $Ti_3C_2T_x$ sample. (a-c) TEM images, (d) The $Ti_3C_2T_x$ SAED pattern.

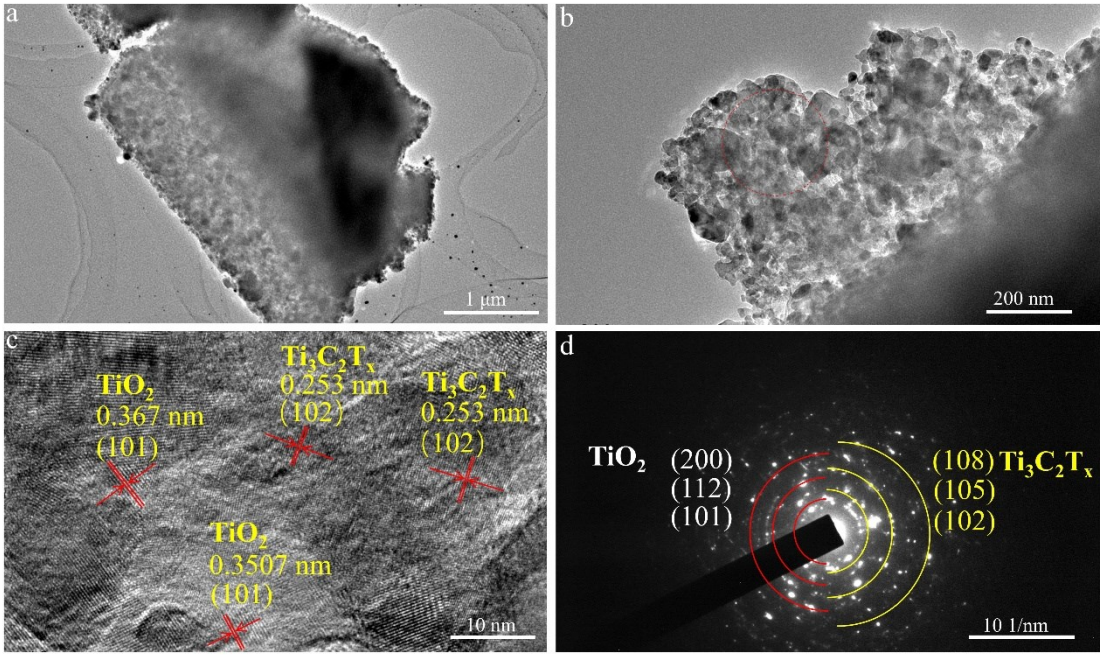

Figure S3 TEM images of $Ti_3C_2T_x$-300 sample. (a-c) TEM images and (d) The $Ti_3C_2T_x$-300 SAED pattern.

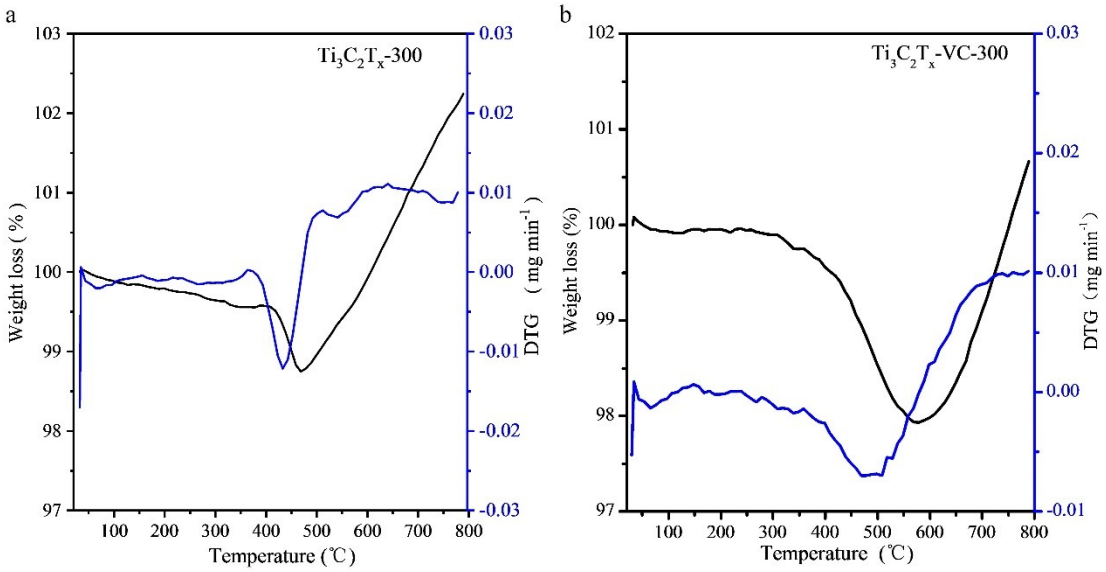

Figure S4 TG-DSC measurement of $Ti_3C_2T_x$-300 (a) and $Ti_3C_2T_x$-VC-300 (b) in N_2.

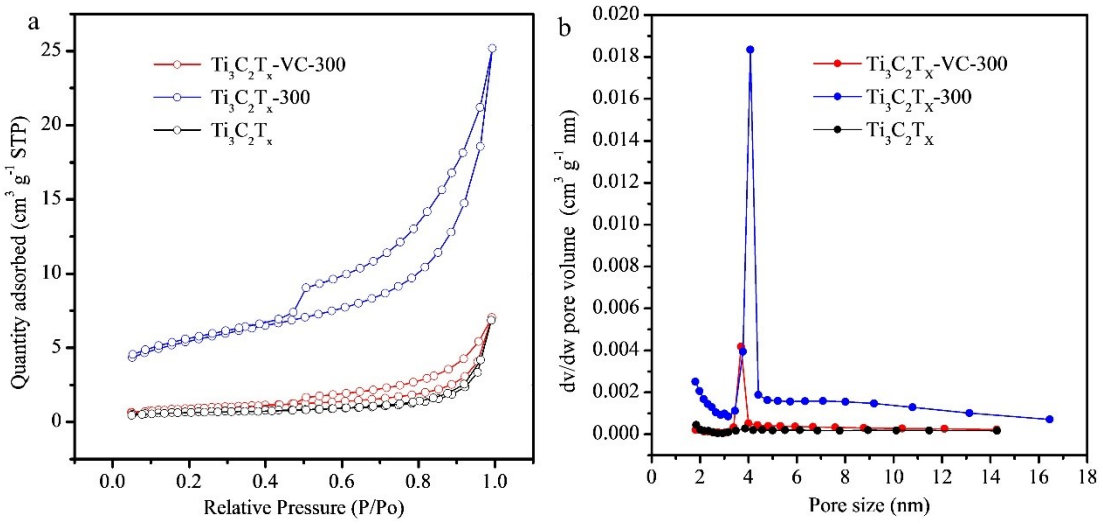

Figure S5 The adsorption-desorption isotherms of $Ti_3C_2T_x$, $Ti_3C_2T_x$-300, $Ti_3C_2T_x$-VC-300 electrodes N_2 (77 K) (a), and their corresponding pore size distribution (b).

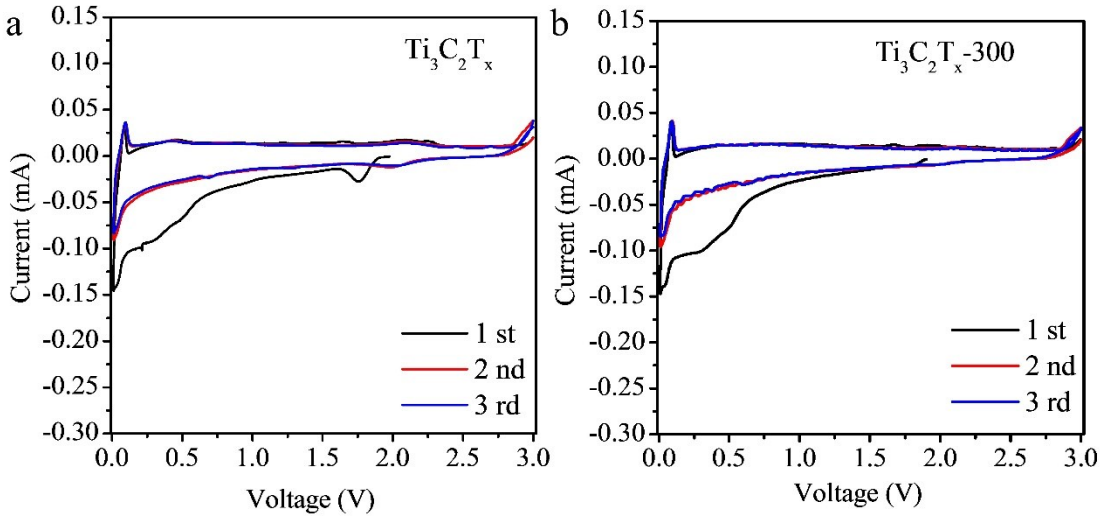

Figure S6 The cyclic voltammogram of electrodes in the first three cycles at 0.1 mV s^{-1}. (a) $Ti_3C_2T_x$ and (b) $Ti_3C_2T_x$-300.

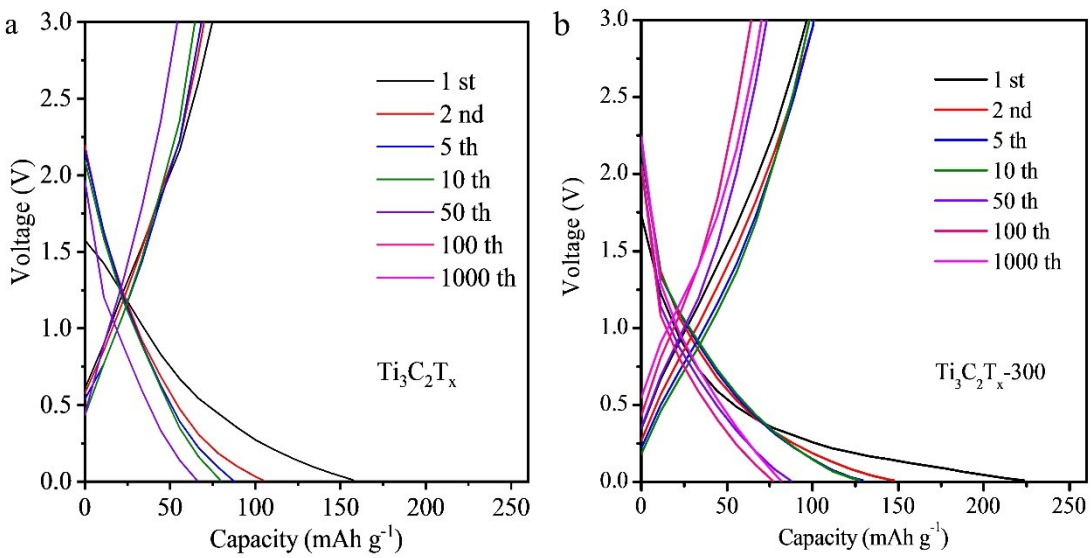

Figure S7 The voltage profile of $Ti_3C_2T_x$ and $Ti_3C_2T_x$-300 electrodes at different cycles. (a) $Ti_3C_2T_x$ and (b) $Ti_3C_2T_x$-300 at 1.0 A g^{-1}.

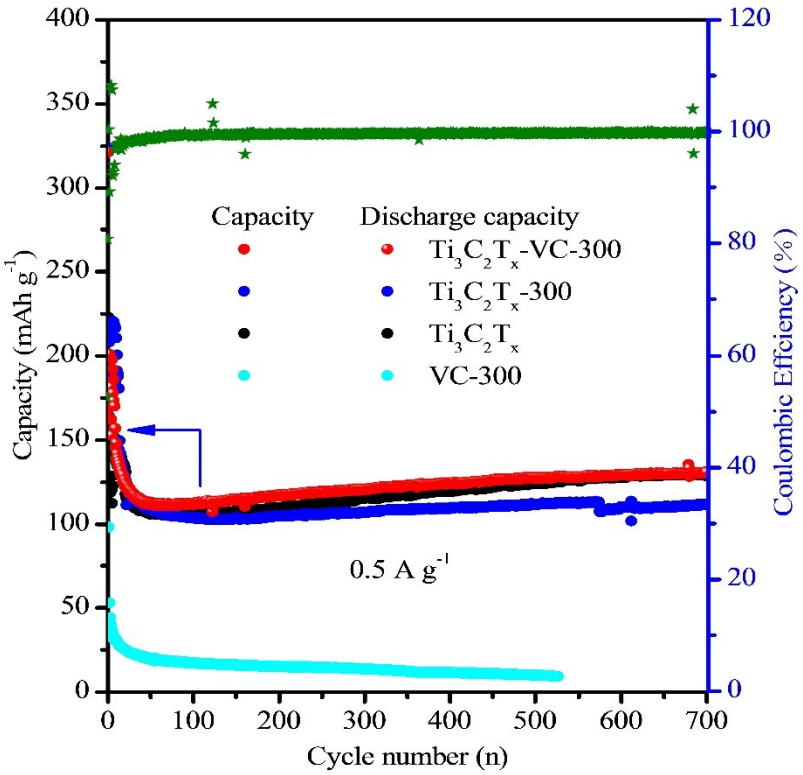

Figure S8 Cycling performance of VC-300, $Ti_3C_2T_x$, $Ti_3C_2T_x$-300 and $Ti_3C_2T_x$-VC-300 electrodes at a current density of 0.5 A g^{-1}.

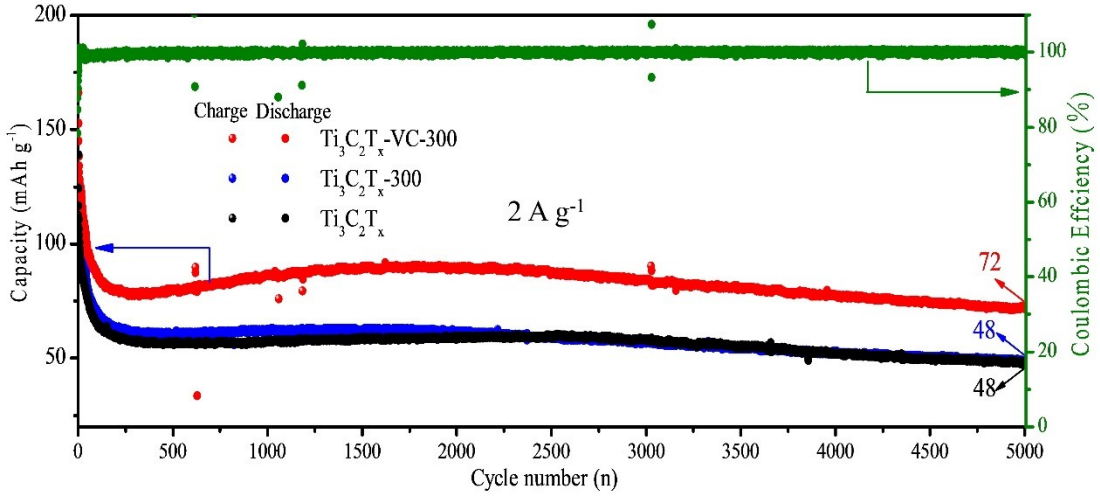

Figure S9 The long cycling performance of $Ti_3C_2T_x$, $Ti_3C_2T_x$-300 and $Ti_3C_2T_x$-VC-300 electrodes at a current density of 2 A g^{-1} after 5000 cycles.

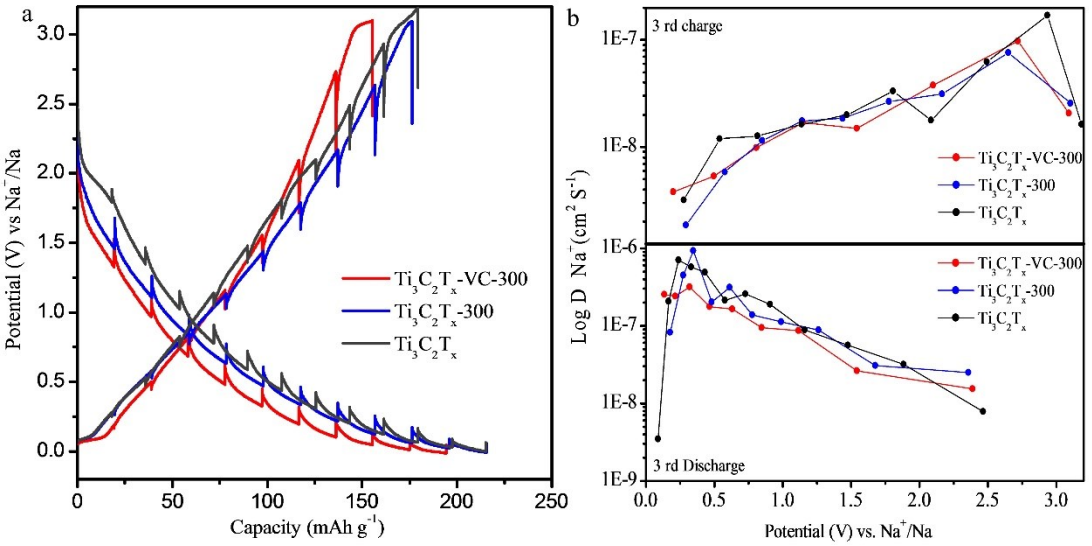

Figure S10 (a) GITT profiles of $Ti_3C_2T_x$, $Ti_3C_2T_x$-300 and $Ti_3C_2T_x$-VC-300 electrodes, (b) Na^+ diffusion coefficients of $Ti_3C_2T_x$, $Ti_3C_2T_x$-300, and $Ti_3C_2T_x$-VC-300 electrodes after the 3rd cycles.

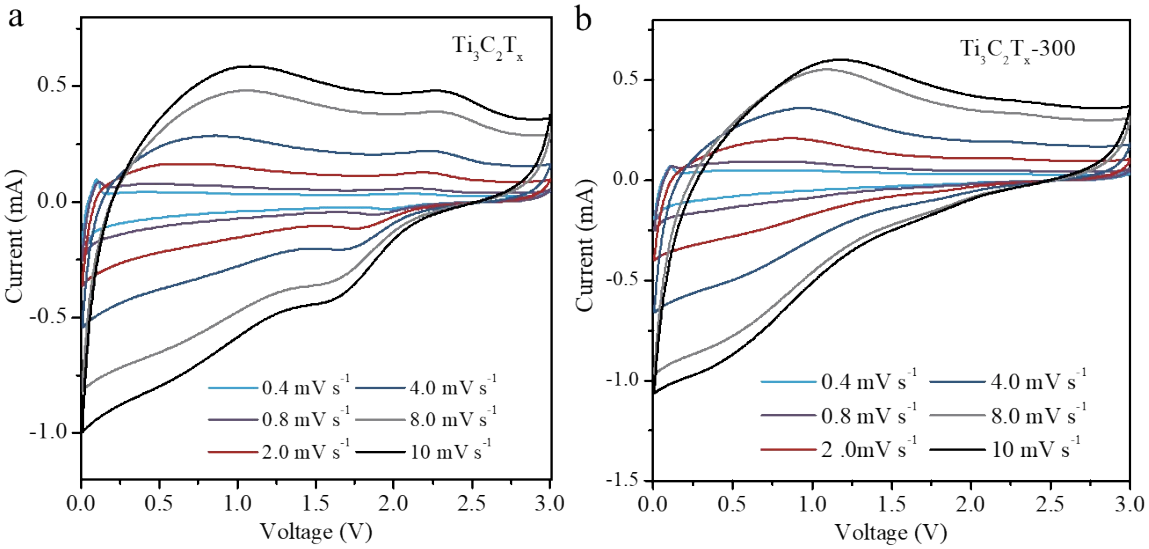

Figure S11 (a) CV curves of $Ti_3C_2T_x$ electrode at different scan rates. (b) CV curves of $Ti_3C_2T_x$-300 electrode at different scan rates.

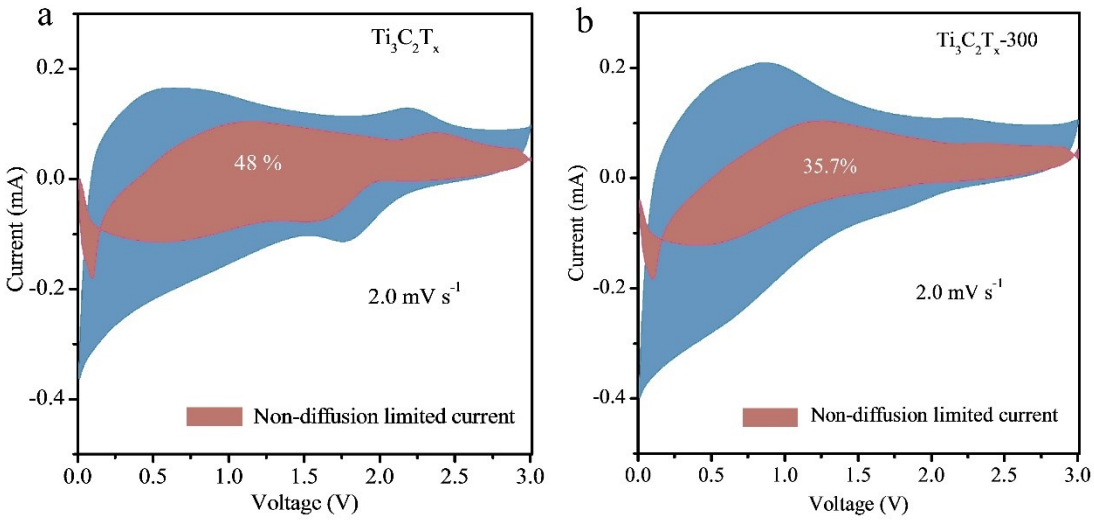

Figure S12 The pseudocapacitive contribution (red and pink region) to the total current of (a) $Ti_3C_2T_x$ and (b) $Ti_3C_2T_x$-300, at a scan rate of 2.0 mV s^{-1}.

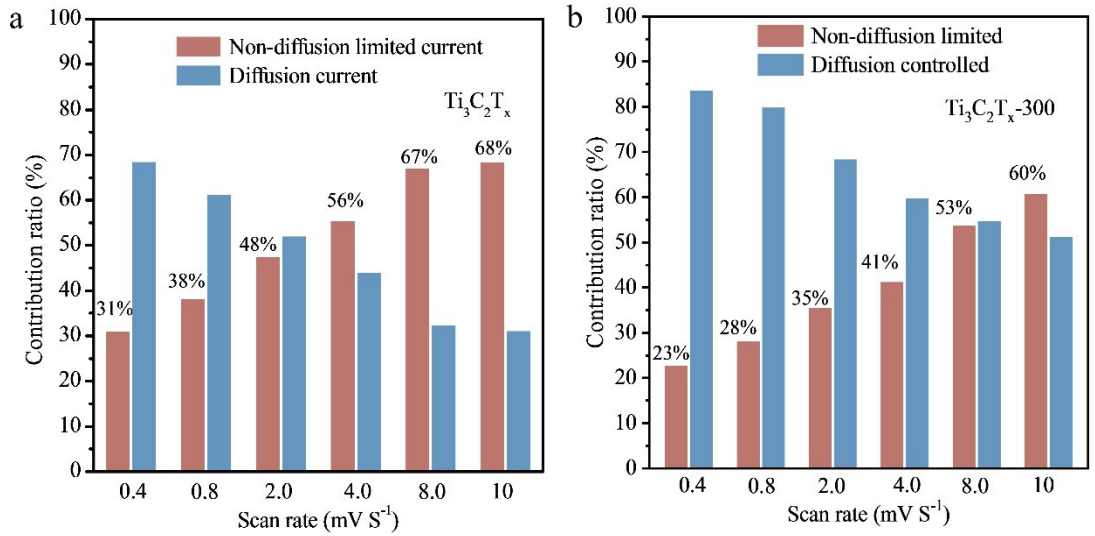

Figure S13 Percentage capacitive contributions obtained at different scan rates of $Ti_3C_2T_x$ (a) and $Ti_3C_2T_x$-300 (b) at a scan rate of 0.4, 0.8, 2.0, 4.0, 8.0 and 10 mV s^{-1}.

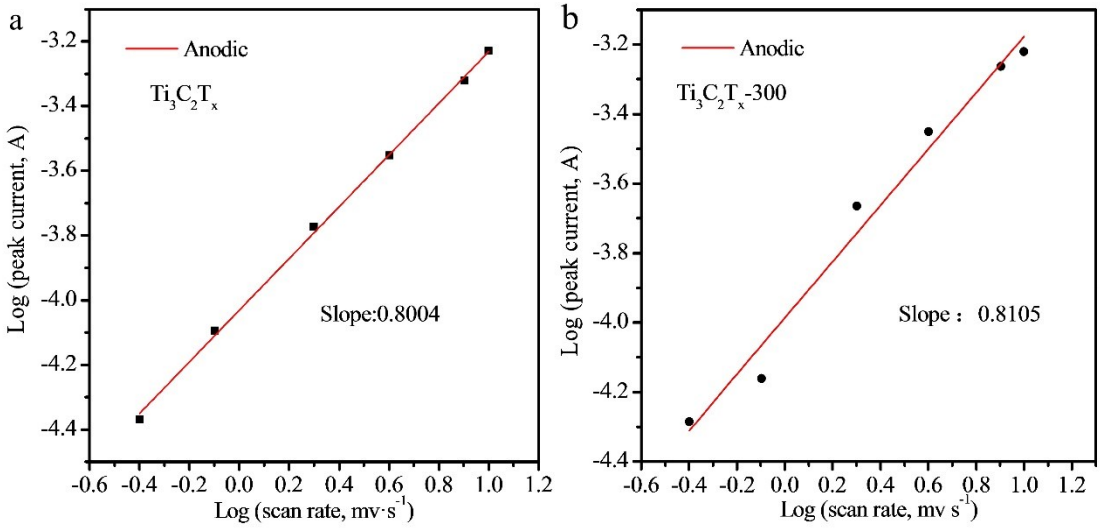

Figure S14 (a) Logarithm peak current versus logarithm scan rate plots of $Ti_3C_2T_x$. (b) Logarithm peak current versus logarithm scan rate plots of $Ti_3C_2T_x$-300.

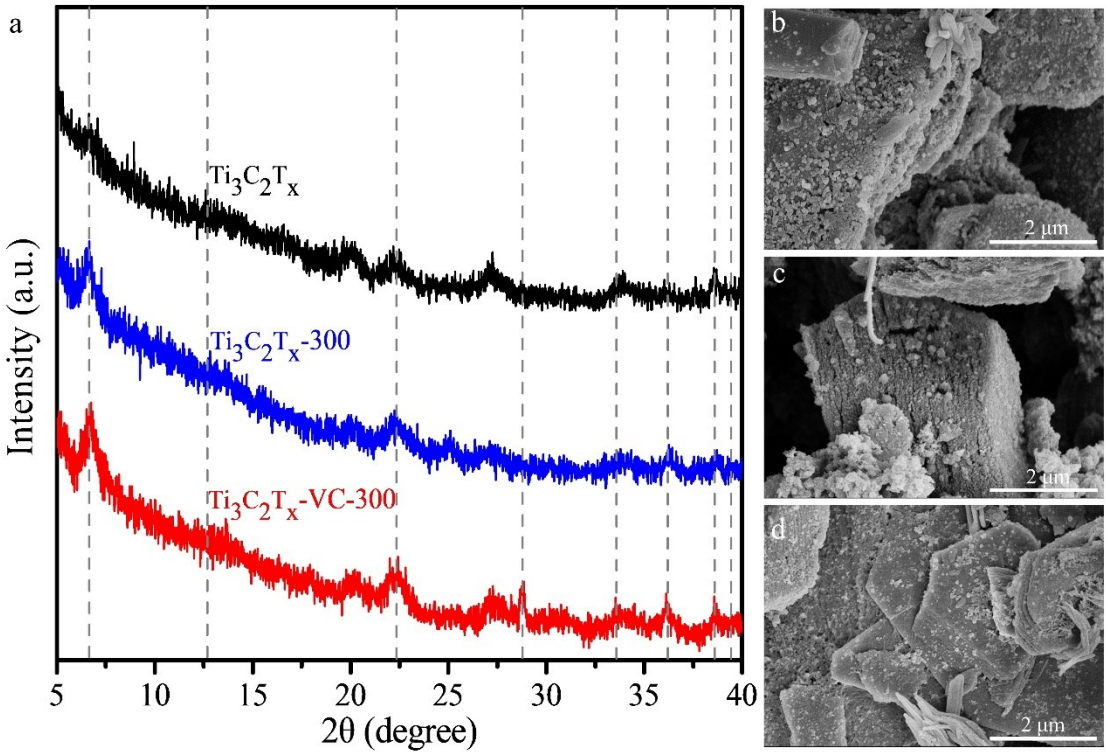

Figure S15 XRD and corresponding SEM images of $Ti_3C_2T_x$, $Ti_3C_2T_x$-300 and $Ti_3C_2T_x$-VC-300 after 50 cycles. (a) XRD images after three electrode cycles, (b) $Ti_3C_2T_x$, (c) $Ti_3C_2T_x$-300, and (d) $Ti_3C_2T_x$-VC-300.

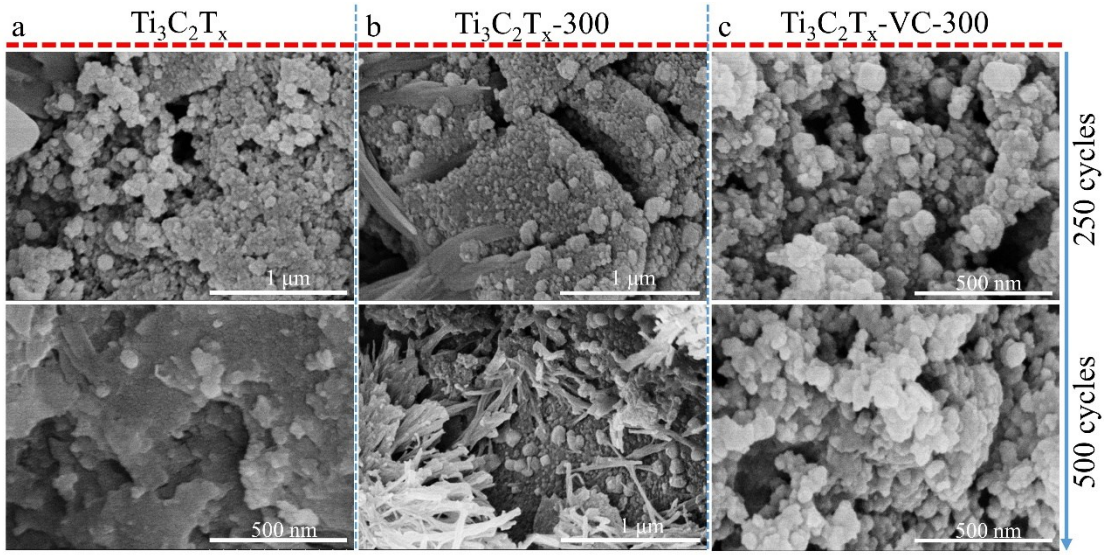

Figure S16 SEM of electrodes after 250 and 500 cycles. (a) $Ti_3C_2T_x$, (b) $Ti_3C_2T_x$-300, and (c) $Ti_3C_2T_x$-VC-300.

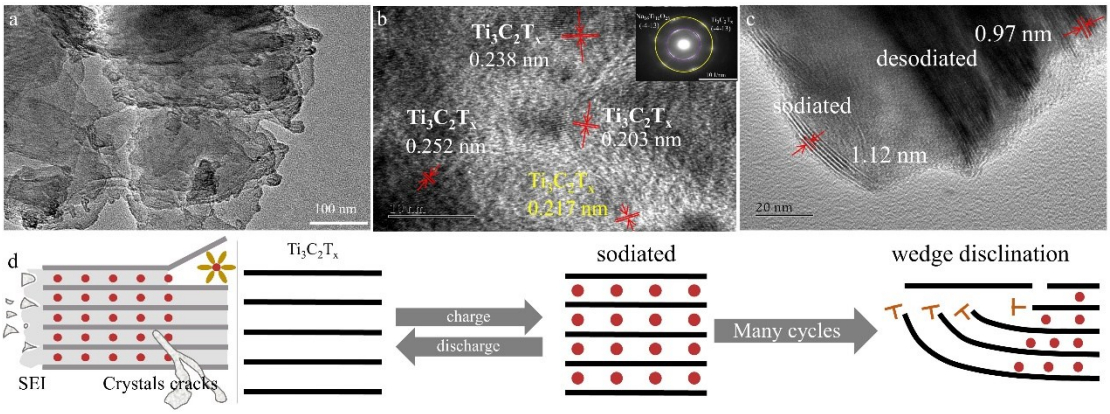

Figure S17 The TEM and capacity decay mechanism of the original $Ti_3C_2T_x$ electrode after 2500 cycles at 1 A g^{-1}. (a) Low magnification TEM image, (b) Medium magnification selected area TEM image, inserting selected area polycrystalline diffraction ring, (c) Side enlarged TEM image, and (d) Schematic diagram of original $Ti_3C_2T_x$ electrode capacity attenuation mechanism.

Supplementary Note 1 | Had $Ti_3C_2T_x$ been successfully obtained by the etching process?

According to our previous results, the samples we obtained after etching Ti_3AlC_2 contain Al, indicating that Al is not completely etched out of the multilayer $Ti_3C_2T_x$. From the crystal structure analysis of MXenes, it is possible to completely etch the Al layer of single-layer MXenes phase unless it is completely etched. The existence of Al leads to some misunderstanding whether MXenes are successfully obtained.

Whether MXenes is successfully obtained or not, the most significant judgment basis and academic consensus is whether MAX precursor is etched to form accordion structure. Therefore, we added FESEM of the original MAX and etched samples (Fig. SN1a-b). The results show that we have successfully obtained multilayer MXenes based on the typical accordion structure feature of MXenes (Fig. SN1b).

In addition, we added the XRD patterns of Ti_3AlC_2 precursor and compared the XRD patterns of the etched samples (Fig. SN1c). Obviously, due to the etching of the Al layer, the crystal structure of the original Ti_3AlC_2 is destroyed, and the crystallinity becomes worse. It is reflected in the XRD patterns that the intensity of the XRD diffraction peak of the etched sample decreases significantly. This shows that we have successfully obtained MXenes from another aspect.

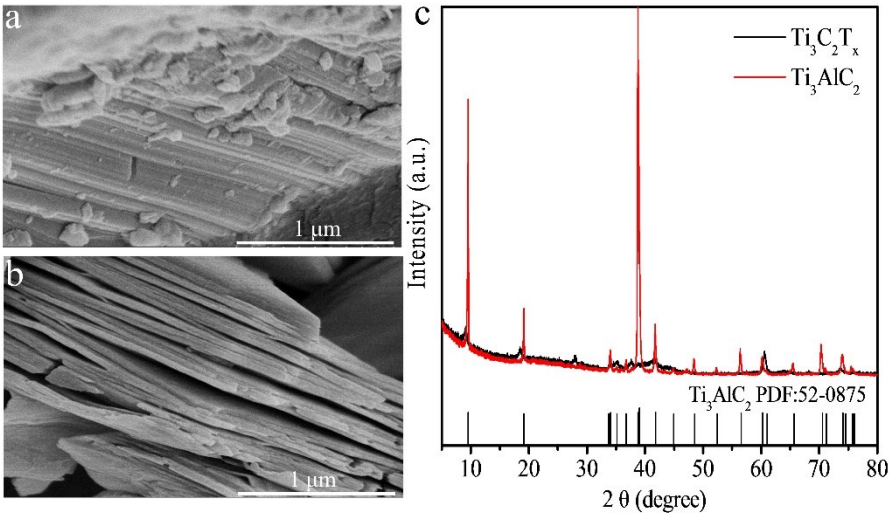

Fig. SN1. (a) Ti_3AlC_2 precursor; (b) etched sample by HF; (c) XRD patterns of Ti_3AlC_2 and $Ti_3C_2T_x$.

Supplementary Note 2 | Have the VC penetrated into the interlayer of MXenes or just coated on the outside surface of the bulk MXenes during the "hot-melting decomposition process?

To investigate whether VC enters the inner surface of $Ti_3C_2T_x$, $Ti_3C_2T_x$ -VC-300 and $Ti_3C_2T_x$ were exfoliated under the same conditions. The FESEM of the peeled samples are shown in Fig. SN2. We found that $Ti_3C_2T_x$ had poor peeling effect, while $Ti_3C_2T_x$-VC-300 had more smaller lamellae after peeling (Fig. SN2a-b). In addition, the surface of $Ti_3C_2T_x$ is smoother than that of $Ti_3C_2T_x$-VC-300 (Fig. SN2c-d). Unfortunately, it is difficult to directly observe the trace of carbon on the surface of $Ti_3C_2T_x$-VC-300. However, based on the analysis of surface roughness of $Ti_3C_2T_x$-VC-300, we think that VC enters the inner surface of $Ti_3C_2T_x$. The reason is that if VC does not enter the inner surface of MXenes, compared with the surface smoothness of $Ti_3C_2T_x$ sample, the surface of MXene-VC-300 should also be smooth. However, the surface of MXene-VC-300 sample is rough. This indirectly proves that VC penetrated the interlayer of MXenes. It should be noted that, it is difficult to judge whether VC enters the sample surface using the mapping measurement of FESEM and TEM, due to and the existence of C in the sample itself.

To sum up, we think that VC are coated on the outer and inner surface of the multilayer MXenes. In view of the problems raised by the reviewer, we have made further analysis and discussion in the supplementary materials.

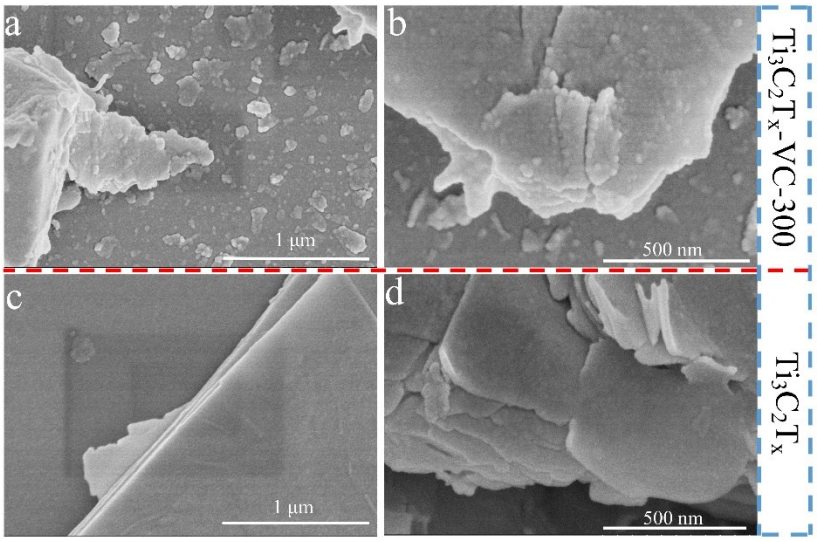

Fig. SN2. The FESEM images of $Ti_3C_2T_x$-VC-300 and $Ti_3C_2T_x$ under the same conditions after peeling and dispersion. (a)-(b) $Ti_3C_2T_x$-VC-300 and (c)-(d) $Ti_3C_2T_x$.

Supplementary Note 3 | Why the pristine $Ti_3C_2T_x$ has the highest carbon ratio?

As we all know, XPS mainly reflects the element composition and chemical environment information of the sample surface with a thickness of 10-20 nm, but it can not reflect the relative content of each element in the whole electrode.

In fact, the carbon content of $Ti_3C_2T_x$ material is higher than that of $Ti_3C_2T_x$-300 material because the structure of $Ti_3C_2T_x$ is destroyed at 300 ℃, resulting in the reaction of carbon in $Ti_3C_2T_x$ in the calcination process; in addition, the partial oxidation of Ti in MXenes to TiO_2 further increases the number of oxygen atoms on the sample surface. The carbon content of $Ti_3C_2T_x$-VC-300 is less than that of $Ti_3C_2T_x$, which is due to the formation of Ti-O bonds when VC decomposes with Ti, and the increase of oxygen atoms on the surface of the material. Based on the above analysis, the relative carbon content of $Ti_3C_2T_x$ is the highest in the three samples. This result further highlights the existence of oxygen rich functional groups on the surface of MXenes.

S2. Tables in supporting information

Table S1. Changes in water contact angle of the $Ti_3C_2T_x$-VC-300 and $Ti_3C_2T_x$-300.

Samples	$Ti_3C_2T_x$	$Ti_3C_2T_x$-300	$Ti_3C_2T_x$-VC-300
Contact Angle		44.99^0	45.43^0
Images	good compatibility (ceramics and metal) difficult for measurement	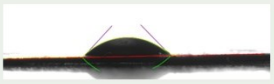	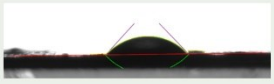

Table S2. Specific surface area (BET), total pore volume and average pore size of $Ti_3C_2T_x$, $Ti_3C_2T_x$-300 and $Ti_3C_2T_x$-VC-300.

Samples	Specific surface area ($m^2\ g^{-1}$)	Pore Volume ($cm^3\ g^{-1}$)	Pore size (nm)
$Ti_3C_2T_x$	2.30	0.0027	6.54
$Ti_3C_2T_x$-300	18.53	0.026	5.58
$Ti_3C_2T_x$-VC-300	3.23	0.0054	5.77

Table S3. The elements percentages of $Ti_3C_2T_x$, $Ti_3C_2T_x$-300 and $Ti_3C_2T_x$-VC-300 measured with XPS.

Samples	Elements (atom contents, %)			
	C	Ti	F	O
$Ti_3C_2T_x$	54.91	16.88	15.60	12.61
$Ti_3C_2T_x$-300	40.52	17.25	7.85	34.37
$Ti_3C_2T_x$-VC-300	45.60	13.89	6.51	34.01

Table S4. Summary table of electrochemical performance of $Ti_3C_2T_x$-based anodes in recent publications.

Anodes	Cycle stability			Ref.
	Current density ($mA\ g^{-1}$)	Cycles (n)	Charge capacity ($mAh\ g^{-1}$)	
This work	1000	2500	153	
Multilayer $Ti_3C_2T_x$ nanosheet	100	120	79	1
Na^+ intercalation $Ti_3C_2T_x$ sheets	20	100	100	2

Alkalized $Ti_3C_2T_x$ nanoribbons	200	500	53	3
Hollow MXene spheres, 3D macroporous MXene frameworks	500	1000	210	4
Few-layer MXenes	1000	1500	76	5
$Ti_3C_2T_x$-derived sodium/potassium titanate nanoribbons	200	150	139	6
Porous $Ti_3C_2T_x$	1000	1000	189	7
3D carbon-coated MXene architectures	1000	3000	139	8
MXene-bonded flexible hard carbon film	200	1500	272	9
Oligolayered $Ti_3C_2T_x$	500	500	280	10
TiO_2@$Ti_3C_2T_x$	960	5000	116	11

Table S5. Electrochemical data derived from EIS spectra for $Ti_3C_2T_x$, $Ti_3C_2T_x$-300 and $Ti_3C_2T_x$-VC-300.

Samples	R_s (Ω)	R_{ct} (Ω)
$Ti_3C_2T_x$	4.6	95.0
$Ti_3C_2T_x$-300	5.1	27.6
$Ti_3C_2T_x$-VC-300	7.0	31.9

Supplementary references

1. Michael Naguib , Vadym N. Mochalin , Michel W. Barsoum and Y. Gogotsi,

25th anniversary article: MXenes: a new family of two-dimensional materials, *Adv. Mater.*, 2014, **26**, 992–1005.

2. S. Kajiyama, L. Szabova, K. Sodeyama, H. Iinuma, R. Morita, K. Gotoh, Y. Tateyama, M. Okubo and A. Yamada, Sodium-ion intercalation mechanism in MXene nanosheets, *ACS Nano*, 2016, **10**, 3334-3341.

3. P. Lian, Y. Dong, Z. Wu, S. Zheng, X. Wang, W. Sen, C. Sun, J. Qin, X. Shi and X. Bao, Alkalized Ti_3C_2 MXene nanoribbons with expanded interlayer spacing for high-capacity sodium and potassium ion batteries, *Nano Energy*, 2017, **40**, 1-8.

4. M. Zhao, X. Xie, C. Ren, T. Makaryan, B. Anasori, G. Wang and Y. Gogotsi, Hollow MXene spheres and 3D macroporous MXene frameworks for Na-ion storage, *Adv. Mater.*, 2017, **29**, 1702410.

5. Y. Wu, P. Nie, J. Wang, H. Dou and X. Zhang, Few-layer MXenes delaminated via high-energy mechanical milling for enhanced sodium-ion batteries performance, *ACS Appl. Mater. Interfaces*, 2017, **9**, 39610-39617.

6. Y. Dong, Z. Wu, S. Zheng, X. Wang, J. Qin, S. Wang, X. Shi and X. Bao, Ti_3C_2 MXene-derived sodium/potassium titanate nanoribbons for high-performance sodium/potassium ion batteries with enhanced capacities, *ACS Nano*, 2017, **11**, 4792-4800.

7. X. Xie, K. Kretschmer, B. Anasori, B. Sun, G. Wang and Y. Gogotsi, Porous $Ti_3C_2T_x$ MXene for ultrahigh-rate sodium-ion storage with long cycle life, *ACS Appl. Mater. Interfaces*, 2018, **1**, 505-511.

8. P. Zhang, R. A. Soomro, Z. Guan, N. Sun and B. Xu, 3D carbon-coated MXene architectures with high and ultrafast lithium/sodium-ion storage, *Energy Storage Mater.*, 2020, **29**, 163-171.

9. N. Sun, Q. Zhu, B. Anasori, P. Zhang, H. Liu, Y. Gogotsi and B. Xu, MXene-bonded flexible hard carbon film as anode for stable Na/K-ion storage, *Adv. Funct. Mater.*, 2019, **29**, 1906282.

10. X. Song, H. Wang, S. Jin, M. Lv, Y. Zhang, X. Kong, H. Xu, T. Ma, X. Luo, H. Tan, D. Hu, C. Deng, X. Chang and J. Xu, Oligolayered $Ti_3C_2T_x$ MXene towards high performance lithium/sodium storage, *Nano Res.*, 2020, **13**, 1659-1667.

11. X. Guo, J. Zhang, J. Song, W. Wu, H. Liu and G. Wang, MXene encapsulated titanium oxide nanospheres for ultra-stable and fast sodium storage, *Energy Storage Mater.*, 2018, **14**, 306-313.